Check for updates

View Article Online
View Journal

Materials Horizons

Accepted Manuscript

This article can be cited before page numbers have been issued, to do this please use: H. Yan, B. Wang, G. Rignanese and Y. Cai, *Mater. Horiz.*, 2026, DOI: 10.1039/D6MH00443A.

This is an Accepted Manuscript, which has been through the Royal Society of Chemistry peer review process and has been accepted for publication.

Accepted Manuscripts are published online shortly after acceptance, before technical editing, formatting and proof reading. Using this free service, authors can make their results available to the community, in citable form, before we publish the edited article. We will replace this Accepted Manuscript with the edited and formatted Advance Article as soon as it is available.

You can find more information about Accepted Manuscripts in the Information for Authors.

Please note that technical editing may introduce minor changes to the text and/or graphics, which may alter content. The journal's standard Terms & Conditions and the Ethical guidelines still apply. In no event shall the Royal Society of Chemistry be held responsible for any errors or omissions in this Accepted Manuscript or any consequences arising from the use of any information it contains.

ROYAL SOCIETY OF CHEMISTRY

rsc.li/materials-horizons

View Article Online
DOI: 10.1039/D6MH00443A

Open Access Article. Published on 11 June 2026. Downloaded on 6/11/2026 11:35:10 PM.
This article is licensed under a Creative Commons Attribution-NonCommercial 3.0 Unported Licence.

We introduce a two-dimensional van der Waals ferroionic heterostructure in which ferroelectric polarization, coupled with local ionic displacements, enables reconfigurable band alignments. Unlike conventional approaches that treat ferroelectricity as a static electrostatic boundary, our strategy exploits ion-driven polarization in $CuInP_2S_6$ (CIPS) as an active and reversible "pump" that modifies interfacial interactions, enabling reversible tuning of band alignment types and carrier transport barriers. A key feature of this mechanism is its strong dependence on the contact environment. Ferroelectric switching in *h*-BN/CIPS is found to induce a type-H to type-II band alignment transition with a reduced barrier, whereas in GR/CIPS, the same switching process leads to a transition from a Schottky contact to a quasi-Ohmic contact, accompanied by bistable polarization switching observed up to 370 K under simulation conditions. The results highlight the coupled role of ionic dynamics and interfacial contacts in governing ferroionic responses, and provide a mechanistic picture for understanding tunable electronic properties in ferroionic heterostructures. These findings suggest the potential for contact-dependent control of interfacial transport characteristics in vdW systems.

Materials Horizons Accepted Manuscript

View Article Online
DOI: 10.1039/D6MH00443A

Open Access Article. Published on 11 June 2026. Downloaded on 6/11/2026 11:35:10 PM.
This article is licensed under a Creative Commons Attribution-NonCommercial 3.0 Unported Licence.

Data availability

Relevant data that support the findings of this study are available in https://github.com/yanhejin/CuInP2S6_Heterostructures.

Materials Horizons Accepted Manuscript

View Article Online
DOI: 10.1039/D6MH00443A

Open Access Article. Published on 11 June 2026. Downloaded on 6/11/2026 11:35:10 PM.
This article is licensed under a Creative Commons Attribution-NonCommercial 3.0 Unported Licence.

Materials Horizons Accepted Manuscript

Ferroionic Heterostructures with Reconfigurable Free-energy Surface and Band Alignment across $CuInP_2S_6$ van der Waals Interface with Boron Nitride and Graphene

Hejin Yan[a†], Bowen Wang[a†], Gian-Marco Rignanese[b], Yongqing Cai[a*]

[a]Institute of Applied Physics and Materials Engineering, University of Macau, Taipa, Macau, 999078, China

[b]Institute of Condensed Matter and Nanosciences, UCLouvain, Louvain-la-Neuve, 1348, Belgium

[*]**Corresponding Author**

[†]**Contribute equally**

ABSTRACT

Two-dimensional ferroelectric semiconductors with nonvolatile polarization hold great promise for next-generation electronics and photovoltaics. Here, we report reconfigurable band alignment in van der Waals heterostructures based on $CuInP_2S_6$ (CIPS) combined with hexagonal boron nitride (*h*-BN) and graphene (GR), arising from coupled ionic displacement and ferroelectric polarization. Driven by the Cu^+ ion-related energy landscape, the ferroelectric polarization order acts as a "pump" that modulates interfacial

View Article Online
DOI: 10.1039/D6MH00443A

Open Access Article. Published on 11 June 2026. Downloaded on 6/11/2026 11:35:10 PM.
This article is licensed under a Creative Commons Attribution-NonCommercial 3.0 Unported Licence.

charge transfer, band alignment configurations, and carrier transport barriers in ferroionic heterostructures. In the *h*-BN/CIPS stack, polarization switching converts the band alignment from type-H to type-II and reduces the switching barrier to ~ 230 meV across the insulating interface. In contrast, in the GR/CIPS heterostructure, it transforms an *n*-type Schottky barrier into a quasi-Ohmic contact while preserving bistable polarization behavior up to 370 K and producing an asymmetric switching potential with a barrier height of ~ 260 meV. These findings highlight the distinct modulation of electronic structure and transport characteristics under different contact environments for ferroionic heterostructures.

INTRODUCTION

Two-dimensional (2D) ferroelectric (FE) materials, possessing tunable polarization field, have attracted significant attention for their ability to modulate carrier densities and enhance anomalous photovoltaic effects.[1-3] Layered materials such as monochalcogenides (SnS, SnSe),[4-6] dichalcogenides ($MoTe_2$, WTe_2),[7, 8] α-In_2Se_3,[9, 10] and $CuInP_2S_6$ (CIPS)[11, 12] exhibit remarkable ionic displacive responses under an electric field. Their intrinsic electric-field-driven ionic ordering provides an additional degree of freedom for modulating the redox potential in FE-based catalysts with tailored catalytic environments [13-15] and offering screening ability for nonvolatile memory.[16-18] Amongst all 2D FE systems, CIPS is unique and highly appealing due to its ideal Curie temperature, which is near room temperature.[19, 20] It exhibits reversible out-of-plane (OOP) polarization controlled by the

Materials Horizons Accepted Manuscript

View Article Online
DOI: 10.1039/D6MH00443A

Open Access Article. Published on 11 June 2026. Downloaded on 6/11/2026 11:35:10 PM.
This article is licensed under a Creative Commons Attribution-NonCommercial 3.0 Unported Licence.

OOP displacements of Cu^{+} cations [21-23] for forming FE states [24, 25], and demonstrates a duality of electric polarization and electric-field-driven high ionic conductivity [26, 27]. Due to its moderate band gap, FE CIPS has been employed in constructing nonvolatile memories [28-31] and in generating bulk photovoltaic effect that potentially surpass the Shockley-Queisser limit [32].

2D ferroelectronic materials typically function in conjunction with other materials by forming heterostructures. The electronic band alignment between 2D ferroelectrics and electrode/nanoalloys (e.g., Au, Cu), or passivating 2D layers (such as hexagonal boron nitride and graphene, hereafter abbreviated as *h*-BN and GR), governs the redox and photoelectric performance of these hybrids.[33] A built-in potential, which is reversible under an external poling field, forms within CIPS upon contact with GR.[32] In a recent study, a polarization-modulated asymmetric potential was revealed in transport measurements at a ~ 10 nm thick GR/CIPS interface.[34] Additionally, integration with monolayer MoS_2 induces strong modulation of second-harmonic generation in CIPS.[35] However, for ferroionic layers like CIPS, the mechanisms by which thermally activated displacive ions—and consequently, the degree of ferroionic ordering—modulate band alignment at the heterointerface remain unclear. Similarly, the effect of the contacting layer on the polarization switching in the FE layer is still poorly understood. While substantial experimental evidence infers the presence of diverse contact behaviors associated with the 2D FE layer,[36] atomic-scale mechanisms correlating ionic disordering with band alignment are lacking.

Materials Horizons Accepted Manuscript

View Article Online
DOI: 10.1039/D6MH00443A

Open Access Article. Published on 11 June 2026. Downloaded on 6/11/2026 11:35:10 PM.
This article is licensed under a Creative Commons Attribution-NonCommercial 3.0 Unported Licence.

In this work, we elucidate the interplay between interfacial charge transfer and reconfigurable polarization across van der Waals (vdW) FE heterolayers. We demonstrate that the CIPS monolayer strongly modifies the band alignment across heterointerfaces formed with *h*-BN or GR through controlling the amount of transferred charge in two FE states. Conversely, the contact layers exert a pronounced influence on Cu^+ ion kinetics in CIPS, significantly renormalizing the free-energy landscapes of Cu^+ switching. Our study reveals that asymmetric double-well potentials emerging in these heterostructures stabilize the FE order of CIPS down to the 2D limit (~ 7 Å), which is crucial for potential electronic applications such as efficient electron-hole separation at CIPS-based heterointerfaces.

RESULTS AND DISSCUSSIONS

Interfacial rigidity modulated by the polarization reversal in CIPS

In a freestanding CIPS, FE polarization is stabilized at temperatures below the Curie point (T_c = 315 K).[37] This polarization arises from the preferential occupation by Cu^+ cations of one of the two symmetrically equivalent and vertically aligned empty sites, within the octahedral unit formed by sulfur that sit on the upper and lower basal planes. From a dynamical perspective, the configurational behaviors of Cu^+ ions can be characterized into two distinct types of motion in CIPS. The first is a local, bistable off-centering displacement of Cu^+ within the $P_2S_6^{2-}$ framework, which gives rise to spontaneous polarization.[38] The stability of these polarization states has been confirmed by first and second-harmonic piezo-response force microscopy (PFM) measurements, with

Materials Horizons Accepted Manuscript

View Article Online
DOI: 10.1039/D6MH00443A

Open Access Article. Published on 11 June 2026. Downloaded on 6/11/2026 11:35:10 PM.
This article is licensed under a Creative Commons Attribution-NonCommercial 3.0 Unported Licence.

Materials Horizons Accepted Manuscript

contributions from electrochemical-strain and electrostatic effect carefully exculuded.[39] The second type corresponding to long-range Cu^+ migration, a nonequilibrium process governed by multiple factors, including the electric field amplitude and cycling history, as well as localized defects and available interlayer migration pathways.[31, 40, 41] In this work, we focus exclusively on the intrinsic equilibrium polar switching of pristine, stoichiometric CIPS monolayer, and further investigate its modulation through interfacial coupling in heterostructures. Our first-principles density functional theory (DFT) simulations are performed through Vienna *ab initio* Simulation Package (VASP),[42] and details are listed in **Section I** and **II** in the **Supporting information**. Switching the polarization direction involves collective displacement of Cu^+ cations from one site type to the other, passing through the high-symmetry midpoint (**Figure 1a**). When stacked with *h*-BN or GR, for discussion purpose, the two polarization states are denoted as the "NEAR" and "FAR" states: in the NEAR state, the occupying Cu^+ cations are close to the *h*-BN or GR layer, whereas in the FAR state, they are situated away from it (**Figure 1b-e**).

In the stacking configurations considered here, the *h*-BN and GR layers serve as inert passivation layers, effectively blocking environmental contaminants (e. g., O_2 and H_2O) and suppressing unintended migration of Cu^+ ions. The binding energy per CIPS formula unit is calculated according to the formula:

$$E_b = (E_{\mathrm{hete}} - E_{\mathrm{CIPS}} - E_{h-\mathrm{BN/GR}})/n \quad (1)$$

where E_{hete}, E_{CIPS}, and $E_{h-\mathrm{BN/GR}}$ are the energies of total heterostructure, isolated CIPS monolayer, and isolated passivation layer (*h*-BN or GR monolayer) respectively, and n represents the number of CIPS formula units in the heterostructure. For both *h*-BN and GR

View Article Online
DOI: 10.1039/D6MH00443A

Open Access Article. Published on 11 June 2026. Downloaded on 6/11/2026 11:35:10 PM.
This article is licensed under a Creative Commons Attribution-NonCommercial 3.0 Unported Licence.

based heterostructures (**Figure 1f, g**), the NEAR state exhibits stronger interlayer binding: E_b at equilibrium configuration are -566.7 meV (NEAR state) and -477.5 meV (FAR state) for *h*-BN/CIPS, with a discrepancy of 89.2 meV; for GR/CIPS, E_b are -566.4 meV (NEAR state) and -494.8 meV (FAR state), with a difference of 71.6 meV. For both types of heterostructures, the interlayer interactions are dominated by weak vdW forces and are highly sensitive to the polarization states of CIPS.

Materials Horizons Accepted Manuscript

View Article Online
DOI: 10.1039/D6MH00443A

Open Access Article. Published on 11 June 2026. Downloaded on 6/11/2026 11:35:10 PM.
This article is licensed under a Creative Commons Attribution-NonCommercial 3.0 Unported Licence.

Figure 1. (a) Schematic illustration of switchable polarization states in CIPS: the NEAR state corresponds to the upward displacement of Cu^{+} cations close to the passivation layer, and conversely for the FAR state. Arrows indicate the direction of polarization in CIPS (P↑ and P↓ for NEAR and FAR states, respectively). Top views (b, c) and side views (d, e) of the *h*-BN/CIPS and GR/CIPS heterostructures. The interlayer binding energy of *h*-BN/CIPS (f) and GR/CIPS (g) heterostructures as a function of interlayer distance (Δd). The discrete solid circles denote energy values from DFT calculations; solid lines represent fitted curves based on the Buckingham potential.

The interlayer interaction energies of these heterostructures are fitted using the Buckingham and Lennard-Jones (LJ) potentials:[43, 44]

$$E_{b,\,\mathrm{Buckingham}} = ae^{-b\Delta d} - c/\Delta d^{6} \tag{2}$$

$$E_{b,\mathrm{LJ}} = 4\varepsilon[(\sigma/\Delta d)^{12} - (\sigma/\Delta d)^{6}] \tag{3}$$

where a, b, c, ε, and σ are fitting parameters, and Δd is the interlayer distance between the CIPS and the passivation layer. In the NEAR state, the equilibrium Δd values corresponding to the lowest-energy configuration are 3.52 Å and 3.54 Å for *h*-BN/CIPS and GR/CIPS, respectively; in the FAR state, these values increase to 3.54 Å and 3.58 Å. Similar results are reproduced in the fitted Lennard-Jones potential (**Figure S1** and **Table S1**). Therefore, *h*-BN/CIPS and GR/CIPS heterostructures are comparable in terms of E_b magnitude, both displaying polarization-sensitive interlayer interactions. The reversal of polarization in CIPS effects on the structures of both the CIPS and passivation layers are also given in **Tables S2-S4** and **Section III** in the **Supporting information**.

Materials Horizons Accepted Manuscript

View Article Online
DOI: 10.1039/D6MH00443A

Open Access Article. Published on 11 June 2026. Downloaded on 6/11/2026 11:35:10 PM.
This article is licensed under a Creative Commons Attribution-NonCommercial 3.0 Unported Licence.
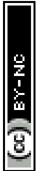

Additionally, the interfacial elastic constant (C_{33}) associated with the deformation vdW gap is derived *via* $C_{33} = \frac{\Delta d_0}{S}\frac{\partial^2 E_b}{\partial \Delta d^2}$, where Δd_0 is the equilibrium distance determined in the Δd–E_b curve and S is the area of the supercell. The fitted C_{33} value for h-BN/CIPS is slightly larger than that for GR/CIPS (**Table S5**). Interestingly, reversing the polarization states in CIPS tunes C_{33}, dropping from 14.3 GPa (NEAR state) to 10.7 GPa (FAR state) for *h*-BN/CIPS, and from 11.3 GPa (NEAR state) to 10.4 GPa (FAR state) for GR/CIPS; all values are much weaker than that of graphite (38 GPa). The observed softening of interlayer interactions in the FAR state arises from diminished electron density within the vdW gaps, indicating the possibility of achieving tunable structural flexibility by poling the surface of the heterostructure. The tunable C_{33} of CIPS-based heterostructures highlights an efficient electromechanical response.

Proximity effect and interlayer charge transfer across CIPS and *h*-BN or GR

Upon contacting CIPS with *h*-BN or GR, a redistribution of charges occurs across both layers. The charge transfer is quantified through the planar-averaged differential charge density $\Delta\rho = \rho_{\mathrm{hete}} - \rho_{\mathrm{CIPS}} - \rho_{h-\mathrm{BN/GR}}$ and the transferred charge (ΔQ):[45, 46]

$$\Delta Q(z) = \int_0^Z \Delta\rho(z)\, dz \qquad (4)$$

where ρ_{hete} is the charge density of the heterostructure, ρ_{CIPS} and $\rho_{h-\mathrm{BN/GR}}$ denote the charge density of the isolated CIPS monolayer and *h*-BN or GR layer, respectively, and *z* is the vertical distance measured from the bottom of the simulation box. The net transferred

Materials Horizons Accepted Manuscript

View Article Online
DOI: 10.1039/D6MH00443A

charge from h-BN or GR to CIPS corresponds to the value of ΔQ at the nodal (zero-crossing) plane of the $\Delta\rho(z)$ profile within the interfacial region.

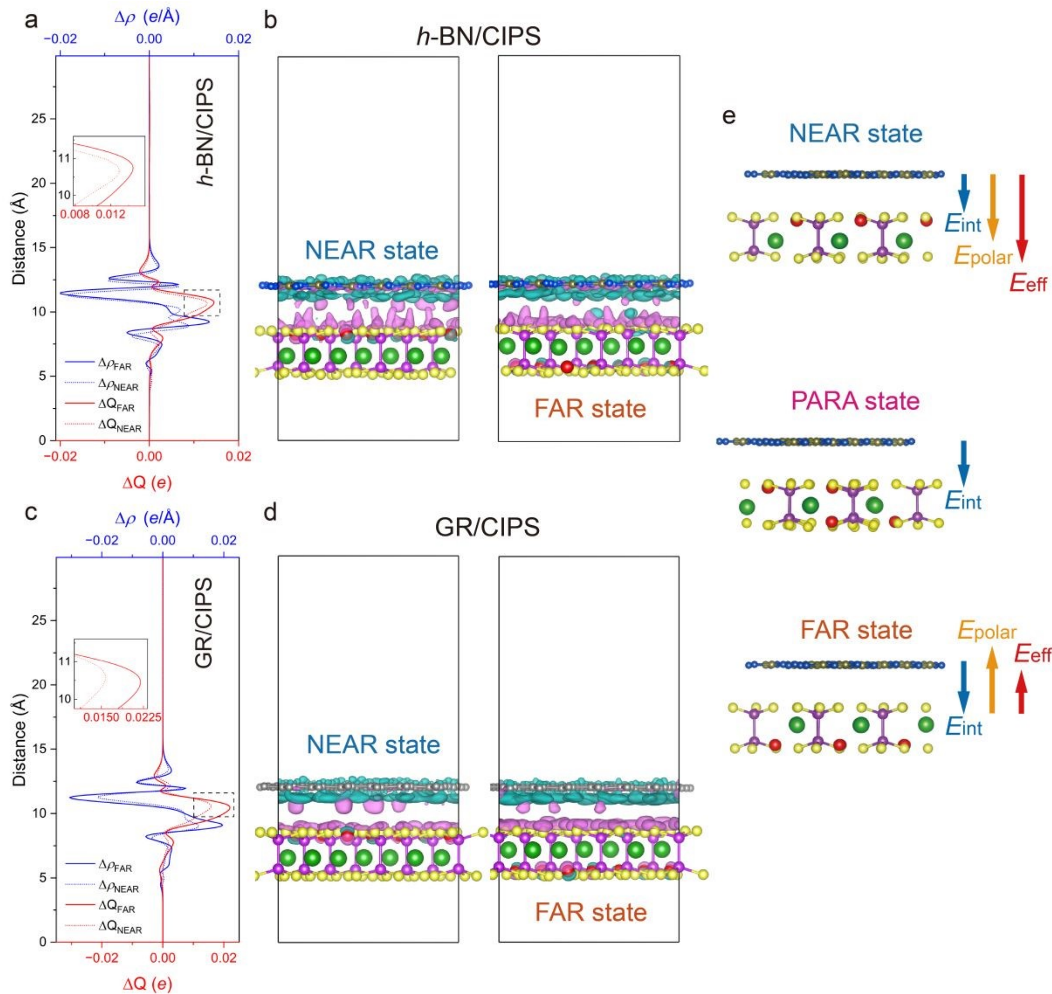

Figure 2. Planar-averaged differential charge density ($\Delta\rho$) and transferred charge (ΔQ) per CIPS formula unit for the h-BN/CIPS (a) and GR/CIPS (c) heterostructures in both FAR and NEAR states. Insets show enlarged views of ΔQ profiles near the interface. Real-space distribution of $\Delta\rho$ for the h-BN/CIPS (b) and GR/CIPS (d) heterostructures in the two polarization states. Iso-surfaces are set at 1.5×10^{-4} $e/\text{Å}^3$ with pink and cyan representing electron accumulation and depletion, respectively. (e) Schematic illustration of the net effective electric field (E_{eff}) resulting from the summation of the built-in interfacial electric

Open Access Article. Published on 11 June 2026. Downloaded on 6/11/2026 11:35:10 PM.
This article is licensed under a Creative Commons Attribution-NonCommercial 3.0 Unported Licence.

Materials Horizons Accepted Manuscript

View Article Online
DOI: 10.1039/D6MH00443A

Open Access Article. Published on 11 June 2026. Downloaded on 6/11/2026 11:35:10 PM.
This article is licensed under a Creative Commons Attribution-NonCommercial 3.0 Unported Licence.

field (E_{int}) arising from charge transfer and the polarization field (E_{polar}) induced by the Cu^{+} ferroic ordering.

As shown in **Figure 2a, c**, electrons transfer from the *h*-BN or GR side to the CIPS side upon integration, with GR exhibiting a stronger charge donation ability than *h*-BN, regardless of polarization states of CIPS. This may account for the stronger interlayer interactions between GR and CIPS (**Figure 1g**). In the case of *h*-BN/CIPS, CIPS in the FAR state tends to attract more electrons (1.45×10^{-2} e per CIPS formula unit) than in the NEAR state (1.30×10^{-2} e per CIPS formula unit). This indicates that the Cu^{+} ions at a greater separation from *h*-BN attract more electrons to the CIPS side (red lines in **Figure 2a, b**). A similar trend is observed for GR/CIPS (**Figure 2c, d**), where electron transfer in the FAR state is 2.20×10^{-2} e per CIPS formula unit, higher than in the NEAR state (1.58×10^{-2} e per CIPS formula unit)—approximately 50% and 20% greater than those in the *h*-BN/CIPS case, respectively. Therefore, integrating CIPS with *h*-BN or GR effectively induces *n*-type doping in CIPS and *p*-type doping on the *h*-BN or GR side. In short, the Cu^{+} ions, with their positions and ordering controlled by temperature and external electric field, act as an effective "pump" to regulate the amount of transferred charge to CIPS.

Charge transfer across the interface induces an interfacial electric field (E_{int}), pointing from *h*-BN or GR toward CIPS, thereby generating a built-in potential in both *h*-BN/CIPS and GR/CIPS heterostructures. This induced field is highly localized, as the charge transfer region is largely restricted to the vicinity of the vdW gap (**Figure 2b, d**). In principle, this

Materials Horizons Accepted Manuscript

View Article Online
DOI: 10.1039/D6MH00443A

Open Access Article. Published on 11 June 2026. Downloaded on 6/11/2026 11:35:10 PM.
This article is licensed under a Creative Commons Attribution-NonCommercial 3.0 Unported Licence.

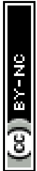

localized and well oriented E_{int} is superimposed on the intrinsic polarization field (E_{polar}) associated with the displaced Cu^{+} ions within the CIPS backbone. We introduce a net effective electric field (E_{eff}), arising from the combined contribution of E_{int} and E_{polar}, which is highly sensitive to the ordering of Cu^{+} ions. **Figure 2e** schematically illustrates the variation of E_{eff} during the transition from the NEAR state to the FAR state. In the NEAR state, E_{int} aligns with E_{polar}, resulting in a stronger E_{eff}; conversely, in the FAR state, E_{polar} oppose E_{int}, leading to a reduced E_{eff}. For comparison, the paraelectric (PARA) state of CIPS in heterostructures is also considered (note: the PARA state has been referred to as the antiferroelectric state in other studies[47, 48]). **Figure S2** shows the structures of *h*-BN/CIPS-PARA and GR/CIPS-PARA states, where Cu^{+} ions are randomly and uniformly distributed on both the top and bottom docking sites of CIPS. In this case, E_{polar} vanish, and only E_{int} contributes to E_{eff} (**Figure 2e**). Since charge transfer is decisive for both direction and intensity of E_{eff} across the interface, its impact on band alignment, carrier transport, and stability of polarization states are discussed in subsequent sections.

Reversal of polarization for tunable band alignment

Figure 3a-d shows the local density of states (LDOS) across the interfaces of *h*-BN/CIPS and GR/CIPS heterostructures. As shown in **Figure 3a**, for *h*-BN/CIPS in the NEAR state, E_{polar} aligns with E_{int}. This generates a relatively strong E_{eff} that bends the bands of CIPS, lifting the conduction band minimum and valence band maximum of CIPS (denoted as CBM_{CIPS} and VBM_{CIPS}, respectively). Conversely, in the FAR state, the

Materials Horizons Accepted Manuscript

View Article Online
DOI: 10.1039/D6MH00443A

Open Access Article. Published on 11 June 2026. Downloaded on 6/11/2026 11:35:10 PM.
This article is licensed under a Creative Commons Attribution-NonCommercial 3.0 Unported Licence.
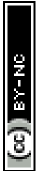

reversed E_{polar} opposes E_{int}, suppressing and even reversing E_{eff}, which lowers the $\mathrm{CBM_{CIPS}}$ and $\mathrm{VBM_{CIPS}}$. In the GR/CIPS heterostructure, a similar trend of band shifting induced by polarization switching is observed (**Figure 3c, d**), where the positions of Cu^+ ions determine the polarization direction and raise (or lower) the band edge states of CIPS near the GR for the NEAR (or FAR) state. In contrast, the PARA state exhibits a more homogeneous distribution of states in CIPS (**Figure S3**), indicating negligible band bending and suppression of E_{polar} within the CIPS layer. Consequently, the band alignment can be effectively tuned depending on which side of the FE CIPS contacts the passivation layer.

Figure S4 gives a schematic representation of band alignment types and corresponding classification of semiconductor heterostructures. For *h*-BN/CIPS in the NEAR state, the interface exhibits type-H band alignment, characterized by substantial band mismatch between the CBM of *h*-BN and CIPS, while the VBM mismatch is negligible (**Figure 3e**). This configuration blocks electron transport from CIPS to *h*-BN while permitting direct hole transport across the interface. Interestingly, polarization switching to the FAR state results in a type-II band alignment at *h*-BN/CIPS, driven by an upward state shifting of *h*-BN, positioning $\mathrm{VBM}_{h-\mathrm{BN}}$ approximately 0.32 eV above $\mathrm{VBM_{CIPS}}$.

Materials Horizons Accepted Manuscript

View Article Online
DOI: 10.1039/D6MH00443A

Open Access Article. Published on 11 June 2026. Downloaded on 6/11/2026 11:35:10 PM.
This article is licensed under a Creative Commons Attribution-NonCommercial 3.0 Unported Licence.

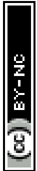

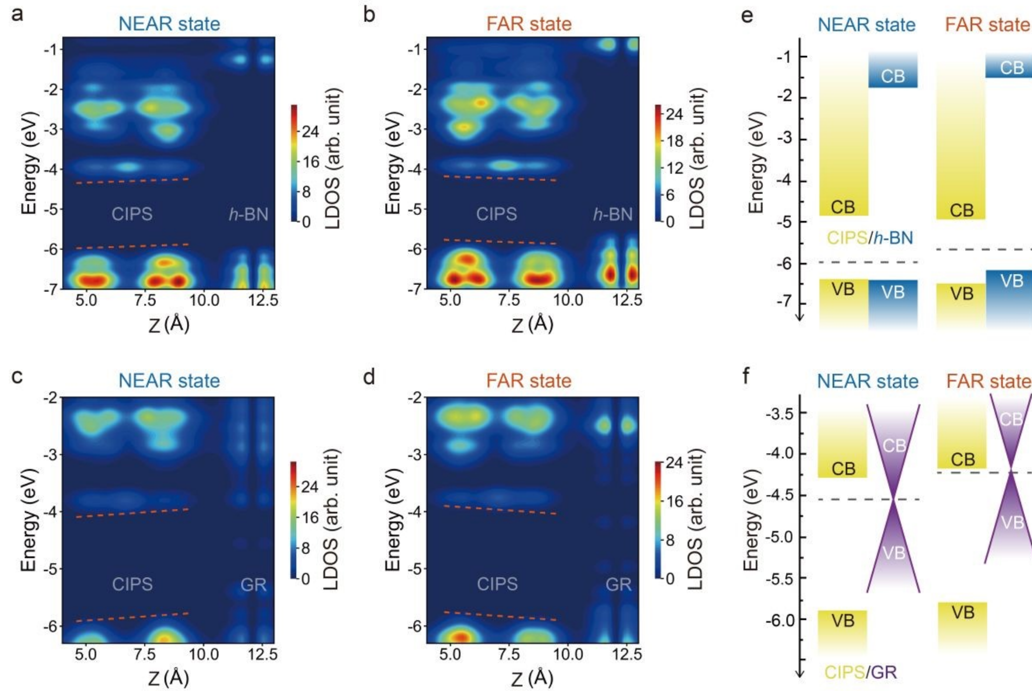

Figure 3. (a, b) LDOS of *h*-BN/CIPS in the NEAR and FAR states, respectively. (c, d) LDOS of GR/CIPS in the NEAR and FAR states, respectively. (e, f) Band diagrams of *h*-BN/CIPS and GR/CIPS heterostructures. The dashed orange lines in (a-d) guide the eye to band bending and tilting within the CIPS layer induced by the interfacial electric field and polarization field. The Fermi level is indicated by horizontal dashed lines in (e) and (f).

In a metal-semiconductor heterostructure, as in the case of GR/CIPS, the relative alignment of Fermi level with the semiconductor band edges determines the contact type formed — either Schottky or Ohmic. For the GR/CIPS-NEAR state, the Fermi level lies within the CIPS band gap, forming a Schottky contact (**Figure 3f**), whereas at the FAR state, a quasi-Ohmic contact emerges. Specifically, there is a substantial band mismatch of ~ 0.27 eV between the Dirac cone and the $\mathrm{CBM_{CIPS}}$ in the NEAR state, which disappears

Materials Horizons Accepted Manuscript

View Article Online
DOI: 10.1039/D6MH00443A

Open Access Article. Published on 11 June 2026. Downloaded on 6/11/2026 11:35:10 PM.
This article is licensed under a Creative Commons Attribution-NonCommercial 3.0 Unported Licence.
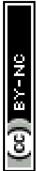

in the FAR state (see **Figure S5c, d**). Therefore, the contacted semi-metallic GR layer is expected to be more sensitive to polarization reversal in CIPS than the insulating *h*-BN. Our findings explain previous experimental observations of tunable *n*-type and *p*-type doping and a substantial Fermi level shift (up to 1 eV) in multilayer CIPS (~ 4 nm thick) upon polarization switching, as confirmed by Kelvin probe force microscopy (KPFM) measurements.[28] More generally, polarization-induced modulation of band alignment is a common phenomenon in FE heterostructures.[49, 50] Here, the term "reconfigurable" specifically refers to the tunability of band alignment induced by FE polarization switching at atomically clean and structurally uniform interfaces, as described within the DFT framework. As summarized in **Table S6**, switching the polarization from the NEAR state to the FAR state transforms the GR/CIPS contact from an *n*-type Schottky to a quasi-Ohmic one, accompanied by a decrease in electron tunneling barrier (Φ_n) and an increase in hole tunneling barrier (Φ_p). The band alignments for the FE and PARA states are also shown in **Figure S6** for comparison.

Apart from the band alignment, the tunneling barrier is another important indicator for interfacial carrier transport. The carrier transport efficiency across the vdW gap is estimated using the tunneling probability (P_{TB}) according to the Simmons formula:[51]

$$P_{\mathrm{TB}} = \exp\left(-\frac{2w_{\mathrm{TB}}}{\hbar}\sqrt{2m\Phi_{\mathrm{TB}}}\right) \tag{5}$$

where w_{TB} and Φ_{TB} are the width and height of the tunneling barrier, and $\hbar$ and m represent the reduced Planck's constant and free-electron mass. The tunneling barriers for *h*-BN/CIPS and GR/CIPS are extracted from the planar-averaged electrostatic potential

Materials Horizons Accepted Manuscript

View Article Online
DOI: 10.1039/D6MH00443A

Open Access Article. Published on 11 June 2026. Downloaded on 6/11/2026 11:35:10 PM.
This article is licensed under a Creative Commons Attribution-NonCommercial 3.0 Unported Licence.

profiles (**Figure S7**). All heterostructures exhibit relatively low tunneling probabilities due to weak orbital overlap across the vdW gap (**Table S7**). The P_{TB} of the *h*-BN/CIPS interface shows pronounced sensitivity to polarization reversal, indicating that *h*-BN/CIPS is promising for nanoelectronics and sensing applications based on tunneling junctions with controllable carrier injection. A recent experiment demonstrated this by fabricating a ferroelectric field-effect transistor (FeFET), where an additional InSe channel integrated atop *h*-BN/CIPS controls the on/off current.[52] The present model corresponds to the ideal vdW contact limit. Although extrinsic inhomogeneities that are likely to occur in real devices—such as those induced by trapped hydrocarbons or fabrication-related disorder—may reduce spatial uniformity, they do not affect the underlying FE-governed interfacial configuration mechanism.

Renormalized dynamics and free-energy landscape of Cu^+ ions in vdW heterostructures

We next show that the addition of passivation layers such as *h*-BN or GR exerts strong effects on ferroic ordering and Cu^+ ion dynamics in CIPS. **Figure S8** compares the total energy of the CIPS monolayer and the heterostructures in different polarization states. For the CIPS monolayer, the PARA state is slightly more energetically favorable (~ 0.04 eV per CIPS formula unit) than the FE state. However, within the heterostructures, the FE NEAR state becomes the ground state, suggesting that interfacial interactions induce a reordering of polarization states in CIPS. The underlying reason is that the interlayer charge transfer compensates and screens the surface polarization bound charges,[53, 54] leading to a

Materials Horizons Accepted Manuscript

View Article Online
DOI: 10.1039/D6MH00443A

Open Access Article. Published on 11 June 2026. Downloaded on 6/11/2026 11:35:10 PM.
This article is licensed under a Creative Commons Attribution-NonCommercial 3.0 Unported Licence.

Materials Horizons Accepted Manuscript

reduction in depolarization energy, especially for the NEAR state, which exhibiting the largest amount of transferred charge to CIPS side.

The probability distribution (p) of Cu^+ species as a function of their relative position along the OOP direction (r_Z) in the CIPS layer, from which free-energy profiles for Cu^+ switching (F, see right panels in **Figure 4a, b**) are extracted as:[55]

$$F(r_Z) = -k_\mathrm{B}T\ln p(r_Z) \tag{6}$$

where k_B is the Boltzmann constant and T is the temperature. For each temperature point, a 10 ps molecular dynamics (MD) is performed in the canonical (NVT) ensemble to maintain the system under isothermal-isochoric condition, and the final 5 ps of the equilibrated trajectories are used to deriving the r_Z distribution. The free-energy barrier heights of Cu^+ switching ($\Delta F = F_\mathrm{NEAR} - F_\mathrm{saddle}$ in heterostructures, or $\Delta F = F_\mathrm{upper} - F_\mathrm{saddle}$ in CIPS monolayer) for transiting between NEAR and FAR states at various temperatures are compiled in **Figure 4c, d** (also see **Table S8** for detailed values). For the freestanding CIPS monolayer, Cu^+ cations exhibit a symmetric free-energy profile and favor equivalent population at both upper and lower sites (**Figure 4c**). Above 330 K, rapid thermally activated Cu^+ switching is triggered, promoting a uniform ion distribution across both facets and indicating that FE states are dynamically unstable in the freestanding CIPS monolayer (**Figure S9**). This observation aligns well with the experimentally determined critical temperature of 315 K for CIPS.[37] It should be emphasized that the activation barriers reported here correspond to Cu^+ off-centering switching between FE states, rather than long-range Cu^+ migration. The former is associated with the reversibility and thermal

View Article Online
DOI: 10.1039/D6MH00443A

response of the reconfigurable band alignment, whereas the latter primarily influences device endurance and leakage behavior in thicker FE systems.[31]

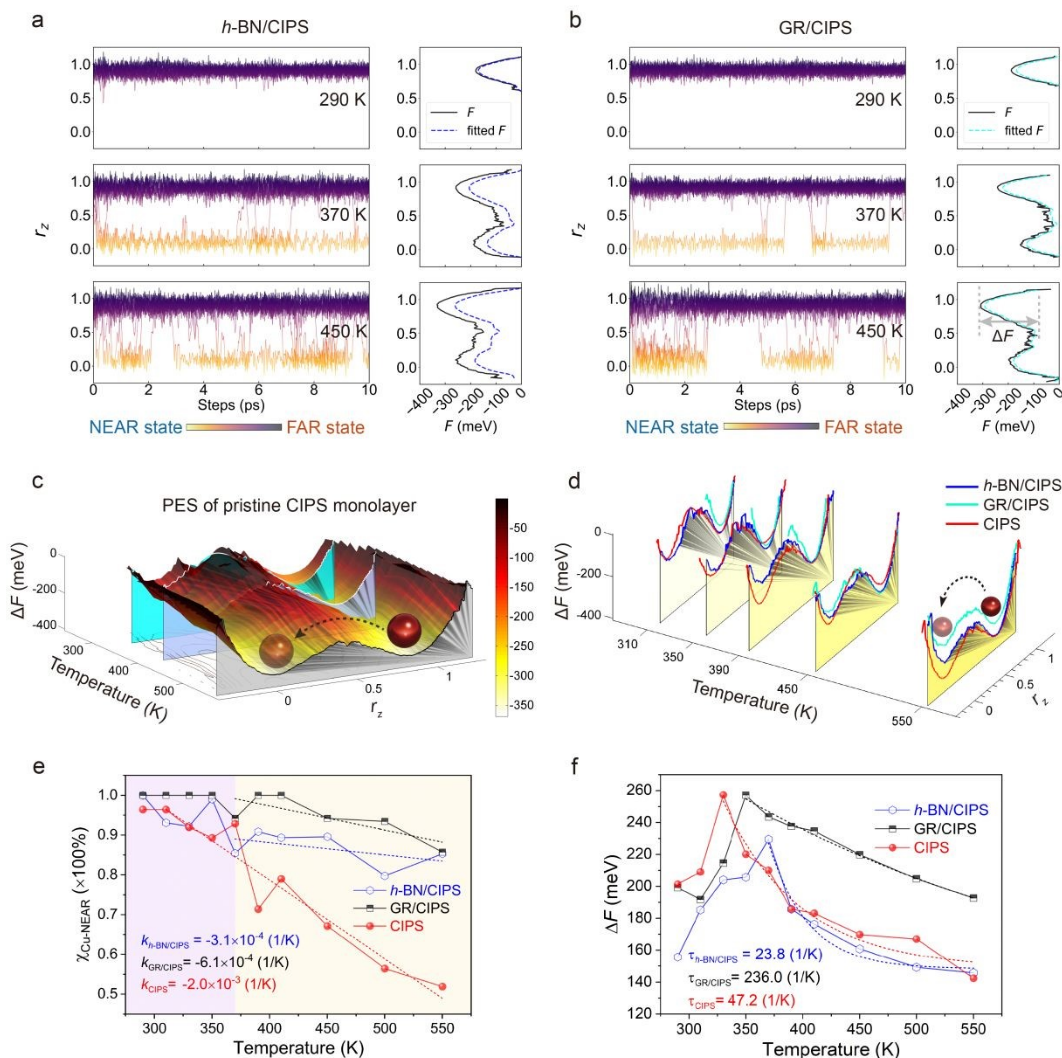

Figure 4. (a, b) Temporal evolution of the relative OOP position of Cu^+ ions in *h*-BN/CIPS and GR/CIPS heterostructures at various temperatures obtained from MD simulations. The right panels show the corresponding free-energy profiles of Cu^+ ions. (c, d) Temperature-dependent potential energy profiles of Cu^+ ions in freestanding CIPS and vdW heterostructures. Asymmetric potential profiles emerge at elevated temperatures in the heterostructures, with NEAR state becoming energetically favorable at larger r_z values. (e)

Open Access Article. Published on 11 June 2026. Downloaded on 6/11/2026 11:35:10 PM.
This article is licensed under a Creative Commons Attribution-NonCommercial 3.0 Unported Licence.

Materials Horizons Accepted Manuscript

View Article Online
DOI: 10.1039/D6MH00443A

Open Access Article. Published on 11 June 2026. Downloaded on 6/11/2026 11:35:10 PM.
This article is licensed under a Creative Commons Attribution-NonCommercial 3.0 Unported Licence.

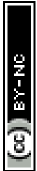

Temperature-dependent $\chi_{\mathrm{Cu-NEAR}}$ exhibits two distinct behaviors: negligible variation below T_c and a rapid decrease above T_c. (f) Temperature-dependent ΔF. Exponential fitting, with fitted decay rate τ, is applied to the data above T_c (≈ 370 K for heterostructures and ≈ 330 K for the CIPS monolayer). The solid and dashed lines in (e) and (f) represent the DFT calculated and fitted values, respectively.

In the *h*-BN/CIPS and GR/CIPS heterostructures, the NEAR state is thermodynamically favored at low temperatures (**Figures S10** and **S13**), consistent with its lower energy compared to the FAR state (**Figure S8b, c**). Furthermore, the potential energy surfaces in these heterostructures are asymmetric (**Figure 4d**), likely due to the built-in electric field E_{int} (**Figure 2**) formed across the interface, which affects F according to the Landau-Ginzburg formula: [56, 57]

$$F = \alpha {P_{polar}}^2 + \beta {P_{polar}}^4 + \gamma {P_{polar}}^6 + \lambda E_{\mathrm{int}} - \varepsilon (P_{polar} \cdot E_{\mathrm{int}}) \quad (7)$$

where α, β, γ, λ, and ε are coefficients, and P_{polar} denotes the dipole moment induced by ionic polar displacement within the CIPS layer. In the NEAR state, P_{polar} is parallel to E_{int}, hence lowering F (ε being positive); whereas in the FAR state, they are antiparallel, thereby elevating F. Additionally, the varying magnitude of E_{int} also contributes to the asymmetric potential surface in these heterostructures (**Figure 2**).

At elevated temperatures, akin to the freestanding case, Cu^+ ions become strongly activated and gradually distribute more uniformly across the top and bottom docking sites (**Figures S10** and **S13**). With the NEAR state as the starting configuration, the proportion

Materials Horizons Accepted Manuscript

View Article Online
DOI: 10.1039/D6MH00443A

Open Access Article. Published on 11 June 2026. Downloaded on 6/11/2026 11:35:10 PM.
This article is licensed under a Creative Commons Attribution-NonCommercial 3.0 Unported Licence.

of Cu^+ ions remaining in the NEAR state (denoted as $\chi_{\mathrm{Cu-NEAR}}$) evolves linearly with temperature, exhibiting two distinct linear regimes: being constant at low temperatures and decreasing linearly at high temperatures, with an inflection point being at $T_c \approx 370$ K for both heterostructures (**Figure 4e**). The fitted slopes at high temperatures are $k_{h-\mathrm{BN/CIPS}} = -3.1 \times 10^{-4}\ \mathrm{K}^{-1}$ and $k_{\mathrm{GR/CIPS}} = -6.1 \times 10^{-4}\ \mathrm{K}^{-1}$ for *h*-BN/CIPS and GR/CIPS, respectively. The enhancement of T_c in both heterostructures compared to freestanding CIPS is attributed to the adhesive binding between *h*-BN or GR and Cu^+ ions, which promotes and stabilizes the FE ordering in heterostructures. Notably, at all temperatures, $\chi_{\mathrm{Cu-NEAR}}$ of GR/CIPS exceeds that of *h*-BN/CIPS, likely due to stronger interfacial binding in the former case (**Figure 1**). Temperature-dependent polarization kinetics are also verified by initializing MD simulations from the FAR and PARA states, yielding the same $T_c \approx 370$ K for both heterostructures (**Figures S11, S12, S14,** and **S15**).

The temperature dependence of ferroionic kinetics is summarized in **Figure 4f**. For all systems, ΔF generally decreases with increasing temperature, and beyond T_c it follows an exponential trend: $\Delta F \propto \exp(-\tau * T)$, where τ is the decay rate. Interestingly, *h*-BN and GR exhibit distinct $T - \Delta F$ characteristics compared with the freestanding CIPS monolayer. For the GR/CIPS heterostructure, the highest ΔF of 257.1 meV occurs at 350 K, and the fitted barrier height (dashed red line) shows a slower decay ($\tau_{\mathrm{GR/CIPS}} = 236.0$ K^{-1}) than that of the CIPS monolayer ($\tau_{\mathrm{CIPS}} = 47.2\ \mathrm{K}^{-1}$). In the *h*-BN/CIPS case, the maximum ΔF (229.5 meV) is less pronounced and occurs at a higher temperature of 370 K (blue point), together with a faster decay ($\tau_{h-\mathrm{BN/CIPS}} = 23.8\ \mathrm{K}^{-1}$, dashed blue line). In

Materials Horizons Accepted Manuscript

View Article Online
DOI: 10.1039/D6MH00443A

Open Access Article. Published on 11 June 2026. Downloaded on 6/11/2026 11:35:10 PM.
This article is licensed under a Creative Commons Attribution-NonCommercial 3.0 Unported Licence.

the low-temperature regime ($T < T_c$), ΔF values in vdW heterostructures are comparable to that of freestanding CIPS monolayer, whereas for high temperatures ($T > T_c$), ΔF for GR/CIPS becomes higher than that of h-BN/CIPS and monolayer CIPS, again due to its relatively stronger interfacial binding.

Previous studies report an energy barrier of ~ 1.1 eV for OOP Cu^+ interlayer migration in CIPS, which enables long-range ion migration in bulk under a strong electric field.[58] For comparison, the corresponding barriers for OOP Cu^+ migration in CIPS-based heterostructures obtained from DFT calculations are shown in **Figure S16a**. In these heterostructures, Cu^+ migration across the vdW gap toward the GR (h-BN) side requires overcoming a barrier of 2.96 eV (4.31 eV), followed by a substantially larger energy increase of 18.45 eV (15.47 eV) associated with penetration into the GR (h-BN) passivation layer. Such extremely high barriers arise from the forced penetration of Cu^+ through pristine, defect-free passivation layers rather than a realistic diffusion pathway. Therefore, cross-interface migration is energetically prohibitive under ideal conditions. Consistently, no long-range Cu^+ migration is observed in MD simulations, indicating that the dynamics are dominated by reversible bistable off-centering rather than ionic diffusion.

We next reveal the correlation and dynamic coupling of Cu^+ species. In **Figure 5a**, the four peaks at 65, 185, 210 and 310 cm^{-1} correspond to in-plane (IP) modes involving Cu^+ atoms, while the 105 cm^{-1} peak corresponds to the OOP polar mode with significant Cu^+ vibration (detailed vibration patterns are given in **Figure S17b**). Adhesion of h-BN or GR does not noticeably affect vibrational peak positions. However, substantial vibrational density of states ($VDOS$) intensity appears at zero frequency for the h-BN/CIPS and

Materials Horizons Accepted Manuscript

View Article Online
DOI: 10.1039/D6MH00443A

Open Access Article. Published on 11 June 2026. Downloaded on 6/11/2026 11:35:10 PM.
This article is licensed under a Creative Commons Attribution-NonCommercial 3.0 Unported Licence.

Materials Horizons Accepted Manuscript

GR/CIPS heterostructures (**Figure 5b, c**), especially at elevated temperatures (> 400 K), indicating diffusive Cu^+ motion likely driven by the interfacial electric field upon stacking *h*-BN or GR. In contrast, this behavior is absent in freestanding CIPS. For both freestanding CIPS and heterostructures, strong peak broadening and reduced intensity occur at elevated temperatures, indicative of phonon anharmonicity. Interestingly, the OOP mode near 105 cm^{-1} strongly broadens and softens with increasing temperatures in freestanding CIPS, while remaining rigid in both heterostructures. Therefore, passivation of 2D vdW heterolayers promotes the flexural stability of Cu^+ species in CIPS.

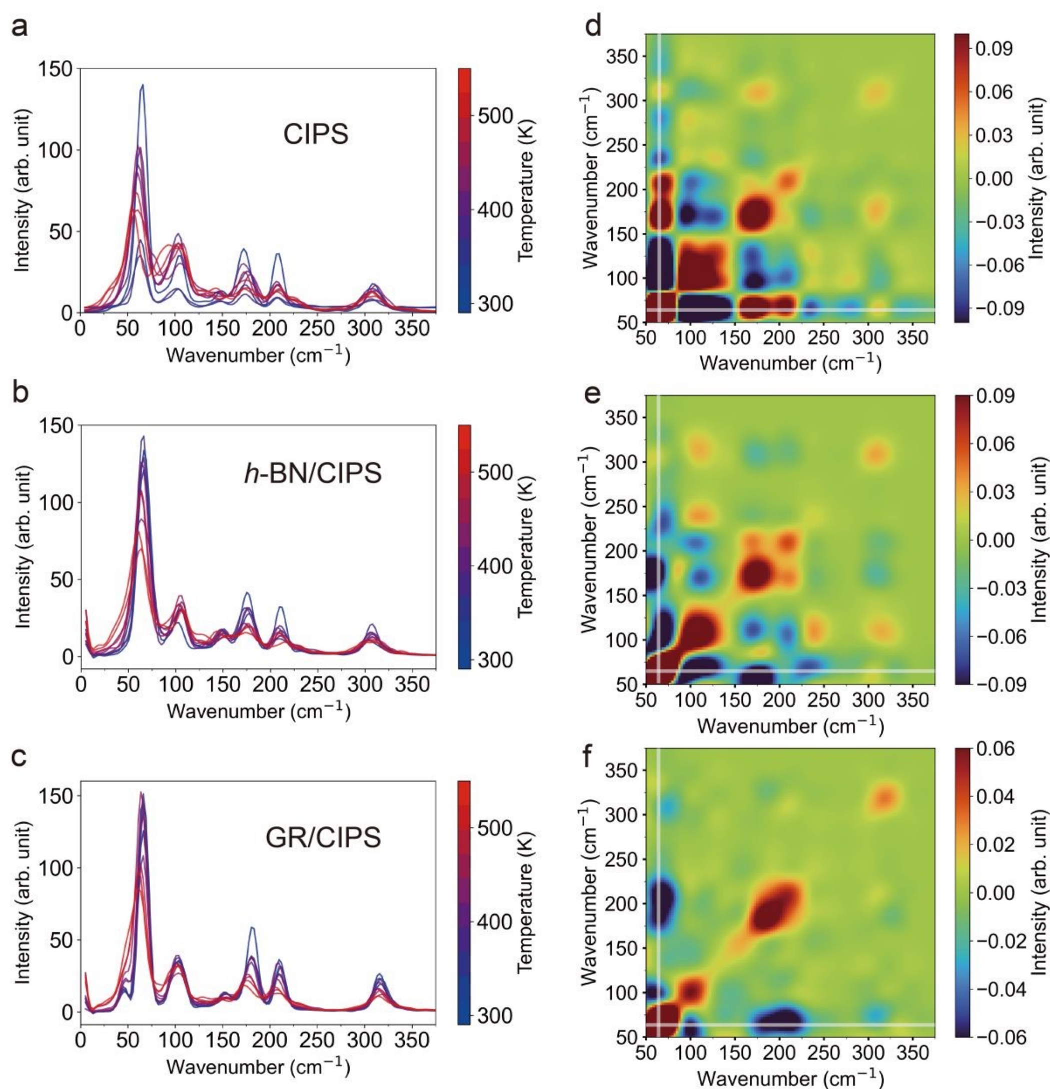

View Article Online
DOI: 10.1039/D6MH00443A

Open Access Article. Published on 11 June 2026. Downloaded on 6/11/2026 11:35:10 PM.
This article is licensed under a Creative Commons Attribution-NonCommercial 3.0 Unported Licence.

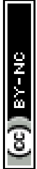

Figure 5. (a-c) $VDOS$ of Cu^+ ions at different temperatures, computed from the velocity autocorrelation function. (d-f) Synchronous 2D correlation spectra of simulated Cu^+ $VDOS$. The off-diagonal regions in red (blue) color indicate positive (negative) correlation between vibrational modes. The white line marks the characteristic peak at 65 cm^{-1}.

Meanwhile, synchronous 2D correlation spectrum analysis is conducted using the temperature-dependent $VDOS$ of Cu atoms, with the averaged synchronous spectrum correlation function (Θ) defined as: [59, 60]

$$\Theta(\omega_1,\omega_2) = \frac{1}{m}\sum_{i=1}^{m} VDOS(\omega_1) \cdot VDOS(\omega_2) \quad (8)$$

where the $VDOS$ data are collected within a time interval $\Delta t = t_{total}/m$, t_{total} is the total simulation time, and m is the number of segments. In the 2D correlation spectrum, the main diagonal contains vibrational modes coupled to themselves (auto peaks), whereas off-diagonal regions represent synchronously or asynchronously linked cross peaks, marked by red (positive value) or blue (negative value) in **Figure 5d-f**. For the CIPS monolayer, the primary peak at 65 cm^{-1} is synchronously coupled with peaks at 185, 210, and 310 cm^{-1} (**Figure 5d**). This is reasonable since all these modes correspond to IP-type Cu motion. Interestingly, these IP modes are asynchronously coupled to the OOP mode at 105 cm^{-1}, but the addition of passivation layers disrupts this synergistic trend. As shown in **Figure 5e**, covering with h-BN layer quenches the coupling between the IP vibration at 65 cm^{-1} with the 185, 210, and 310 cm^{-1} modes, as indicated by the disappearance of the red block spanning 150-225 cm^{-1} that observed in freestanding CIPS (**Figure 5d**). A similar effect

Materials Horizons Accepted Manuscript

View Article Online
DOI: 10.1039/D6MH00443A

Open Access Article. Published on 11 June 2026. Downloaded on 6/11/2026 11:35:10 PM.
This article is licensed under a Creative Commons Attribution-NonCommercial 3.0 Unported Licence.

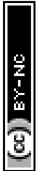

occurs in the GR/CIPS heterostructure, where all off-diagonal regions appear blue, indicating renormalized coupling between FE modes upon the addition of passivation layers. Within the simulation time and temperature window, Cu^+ ions remain confined to the CIPS layer and do not access the vdW gaps or the *h*-BN passivation layer. The results indicate that the reversible modulation of band alignment associated with FE states can occur without long-range ionic migration, while the structural integrity of the heterostructure is preserved under the simulation conditions.

CONCLUSIONS

In summary, we reveal strong charge redistribution and the reshaping of free-energy landscape in ferroionic systems, based on two prototype CIPS-based heterostructures formed with typical passivation layers: the insulating *h*-BN and semi-metallic GR electrodes. The activation of Cu^+ ions and polarization ordering are critical in controlling interlayer interactions, band alignment, carrier transport, and switching barriers. The underlying mechanism involves the coupling between the OOP polarization field of CIPS and the interfacial built-in electric field stemming from interlayer charge transfer. In the *h*-BN/CIPS heterostructure, the type-H band alignment in the NEAR state converts to a type-II configuration in the FAR state, accompanied by a reduced barrier height for Cu^+ switching. In contrast, the GR/CIPS heterostructure undergoes a transition from an *n*-type Schottky contact in the NEAR state to a quasi-Ohmic contact in the FAR state, while enhanced charge transfer elevates the switching barrier. Critically, bistable polarization

Materials Horizons Accepted Manuscript

View Article Online
DOI: 10.1039/D6MH00443A

Open Access Article. Published on 11 June 2026. Downloaded on 6/11/2026 11:35:10 PM.
This article is licensed under a Creative Commons Attribution-NonCommercial 3.0 Unported Licence.

switching behavior is retained up to ~ 370 K under simulation conditions. These findings demonstrate the tunability of electronic properties in ferroionic heterostructures and provide insights into contact-dependent control of carrier transport in vdW systems.

Data availability

Relevant data that support the findings of this study are available in **https://github.com/yanhejin/CuInP2S6_Heterostructures**. Supplementary information: LJ potential fitted distance-energy profiles; Atomic configurations of *h*-BN/CIPS and GR/CIPS at PARA state; Density of states and band structures; Band alignments; Planar-averaged electrostatic potential along out-of-plane direction; Comparison of energy of CIPS monolayer, *h*-BN/CIPS and GR/CIPS heterostructures in different polarization states; Temperature-dependent state switching dynamics and barriers in the CIPS monolayer, *h*-BN/CIPS, and GR/CIPS; Energy barriers for interlayer Cu^+ migration; Phonon dispersion and vibrational density of states in the CIPS monolayer; Stacking energies of the GR/CIPS heterostructure; Section I. Methods of first-principles simulations; Section II. Simulation models; Section III. Polarization switching acting on structures and electronic properties. See DOI:

Author Contributions

Materials Horizons Accepted Manuscript

View Article Online
DOI: 10.1039/D6MH00443A

Hejin Yan planned the project with Yongqing Cai. Hejin Yan designed and performed calculations. This paper was written by Hejin Yan and revised by Bowen Wang and Gian-Marco Rignanese. Hejin Yan and Bowen Wang contribute equally.

Open Access Article. Published on 11 June 2026. Downloaded on 6/11/2026 11:35:10 PM.
This article is licensed under a Creative Commons Attribution-NonCommercial 3.0 Unported Licence.

Conflicts of interest

There are no conflicts of interest to declare.

Acknowledgements

This work is supported by the National Natural Science Foundation of China (22022309), Natural Science Foundation of Guangdong Province, China (2024A1515011161, EF2023-00106-IAPME), the Science and Technology Development Fund from Macau SAR (0122/2024/AFJ, 0120/2023/RIA2) and University of Macau (MYRG-GRG2024-00028-IAPME, MYRG-GRG2025-00045-IAPME). This work was performed in part at the High-Performance Computing Cluster (HPCC), supported by the Information and Communication Technology Office (ICTO) of the University of Macau.

Materials Horizons Accepted Manuscript

REFERENCES

1. S. Deb, W. Cao, N. Raab, K. Watanabe, T. Taniguchi, M. Goldstein, L. Kronik, M. Urbakh, O. Hod and M. Ben Shalom, Nature, 2022, 612, 465-469.
2. S. Li, F. Wang, Y. Wang, J. Yang, X. Wang, X. Zhan, J. He and Z. Wang, Adv. Mater., 2024, 36, 2301472.

View Article Online
DOI: 10.1039/D6MH00443A

Open Access Article. Published on 11 June 2026. Downloaded on 6/11/2026 11:35:10 PM.
This article is licensed under a Creative Commons Attribution-NonCommercial 3.0 Unported Licence.

3. Y. Liu, W. Guo, L. Hua, X. Zeng, T. Yang, Q. Fan, Y. Ma, C. Gao, Z. Sun and J. Luo, J. Am. Chem. Soc., 2023, 145, 16193-16199.
4. E. Sutter, P. Ghimire and P. Sutter, J. Am. Chem. Soc., 2024, 146, 31961-31968.
5. E. Sutter, P. Ghimire and P. Sutter, ACS Nano, 2024, 18, 30829-30837.
6. P. Parajuli, S. Bhattacharya, R. Rao and A. Rao, Mater. Horiz., 2022, 9, 1602-1622.
7. W. Zheng, M. Bonn and H. I. Wang, Nano Lett., 2020, 20, 5807-5813.
8. Y. Zhang, K. Kamiya, T. Yamamoto, M. Sakano, X. Yang, S. Masubuchi, S. Okazaki, K. Shinokita, T. Chen and K. Aso, Nano Lett., 2023, 23, 9280-9286.
9. Y. Zhou, D. Wu, Y. Zhu, Y. Cho, Q. He, X. Yang, K. Herrera, Z. Chu, Y. Han and M. C. Downer, Nano Lett., 2017, 17, 5508-5513.
10. B. Lv, Z. Yan, W. Xue, R. Yang, J. Li, W. Ci, R. Pang, P. Zhou, G. Liu and Z. Liu, Mater. Horiz., 2021, 8, 1472-1480.
11. L. Wang, D. Zhang, Z.-D. Luo, P. D. Taylor, K. Tran, W. Ming, J. Tang, P. Sharma, M. J. Spencer and J. Seidel, Mater. Horiz., 2024, 11, 6486-6496.
12. S. Zhou, L. You, A. Chaturvedi, S. A. Morris, J. S. Herrin, N. Zhang, A. Abdelsamie, Y. Hu, J. Chen and Y. Zhou, Mater. Horiz., 2020, 7, 263-274.
13. L. Ju, Y. Ma, X. Tan and L. Kou, J. Am. Chem. Soc., 2023, 145, 26393-26402.
14. L. Ju, X. Tan, X. Mao, Y. Gu, S. Smith, A. Du, Z. Chen, C. Chen and L. Kou, Nat. Commun., 2021, 12, 5128.
15. W. Shao, Z. Xing, X. Xu, D. Ye, R. Yan, T. Ma, Y. Wang, Z. Zeng, B. Yin and C. Cheng, J. Am. Chem. Soc., 2024, 146, 27486-27498.
16. F. Sun, H. Xu, Q. Ju, W. Hong, Q. Cai, Z. Sun and W. Liu, J. Am. Chem. Soc., 2025, 147, 26804-26812.

Materials Horizons Accepted Manuscript

View Article Online
DOI: 10.1039/D6MH00443A

17. K.-F. Luo, Z. Ma, D. Sando, Q. Zhang and N. Valanoor, ACS Nano, 2025, 19, 6622-6647.
18. X. Yu, L. Xu, W. Shi, X. Meng, X. Huang, Z. Peng, L. Tong, H. Sun, X. Miao and L. Ye, Mater. Horiz., 2025, 12, 8409-8429.
19. F. Liu, L. You, K. L. Seyler, X. Li, P. Yu, J. Lin, X. Wang, J. Zhou, H. Wang and H. He, Nat. Commun., 2016, 7, 1-6.
20. W. Ming, B. Huang, S. Zheng, Y. Bai, J. Wang, J. Wang and J. Li, Sci. Adv., 2022, 8, eabq1232.
21. V. Maisonneuve, V. Cajipe, A. Simon, R. Von Der Muhll and J. Ravez, Phys. Rev. B, 1997, 56, 10860.
22. Y. M. Vysochanskii, V. Stephanovich, A. Molnar, V. Cajipe and X. Bourdon, Phys. Rev. B, 1998, 58, 9119.
23. S. N. Neal, S. Singh, X. Fang, C. Won, F.-t. Huang, S.-W. Cheong, K. M. Rabe, D. Vanderbilt and J. L. Musfeldt, Phys. Rev. B, 2022, 105, 075151.
24. S. M. Yang, A. N. Morozovska, R. Kumar, E. A. Eliseev, Y. Cao, L. Mazet, N. Balke, S. Jesse, R. K. Vasudevan and C. Dubourdieu, Nat. Phys., 2017, 13, 812-818.
25. A. N. Morozovska, E. A. Eliseev, N. V. Morozovsky and S. V. Kalinin, Phys. Rev. B, 2017, 95, 195413.
26. L. Liang, E. Pan, G. Cao, J. Chen, R. Wang, B. Dong, Q. Liu, X. Chen, X. Luo and Y. Kong, Nat. Commun., 2025, 16, 4462.
27. W. Ci, P. Wang, W. Xue, H. Yuan and X. Xu, Adv. Funct. Mater., 2024, 34, 2316360.
28. J. Wu, H.-Y. Chen, N. Yang, J. Cao, X. Yan, F. Liu, Q. Sun, X. Ling, J. Guo and H. Wang, Nat. Electron., 2020, 3, 466-472.

Open Access Article. Published on 11 June 2026. Downloaded on 6/11/2026 11:35:10 PM.
This article is licensed under a Creative Commons Attribution-NonCommercial 3.0 Unported Licence.

Materials Horizons Accepted Manuscript

View Article Online
DOI: 10.1039/D6MH00443A

Open Access Article. Published on 11 June 2026. Downloaded on 6/11/2026 11:35:10 PM.
This article is licensed under a Creative Commons Attribution-NonCommercial 3.0 Unported Licence.

29. L. Zhao, Y. Liang, J. Ma, Z. Pan, X. Liu, M. Yang, Y. Sun, W. Gao, B. Li and J. Li, Adv. Funct. Mater., 2023, 33, 2306708.
30. M. Si, P.-Y. Liao, G. Qiu, Y. Duan and P. D. Ye, ACS Nano, 2018, 12, 6700-6705.
31. Z. Zhong, S. Wu, X. Li, Z. Wang, Q. Yang, B. Huang, Y. Chen, X. Wang, T. Lin and H. Shen, ACS Nano, 2023, 17, 12563-12572.
32. Y. Li, J. Fu, X. Mao, C. Chen, H. Liu, M. Gong and H. Zeng, Nat. Commun., 2021, 12, 5896.
33. C. Tan, H. Wu, Z. Lin, L. Yang and Z. Wang, Adv. Funct. Mater., 2025, 35, 2415360.
34. S. Sarkar, Z. Han, M. A. Ghani, N. Strkalj, J. H. Kim, Y. Wang, D. Jariwala and M. Chhowalla, Nano Lett., 2024, 24, 13232-13237.
35. D. Li, X. Hou, F. Kong, K. Wang and X. Hong, ACS Nano, 2024, 18, 32890-32898.
36. J. Cheng, P. Zhang, X. Ouyang, W. Tang, B. Song, Y. Zhang, Y. Zheng and A. Pan, Adv. Funct. Mater., 2025, 35, 2416333.
37. M. Si, A. K. Saha, P.-Y. Liao, S. Gao, S. M. Neumayer, J. Jian, J. Qin, N. Balke Wisinger, H. Wang and P. Maksymovych, ACS Nano, 2019, 13, 8760-8765.
38. W. Song, R. Fei and L. Yang, Phys. Rev. B, 2017, 96, 235420.
39. L. Wang, D. Zhang, Z. D. Luo, P. Sharma and J. Seidel, Adv. Funct. Mater., 2023, 33, 2303583.
40. H. Zhu, J. Li, Q. Chen, W. Tang, X. Fan, F. Li and L. Li, ACS Nano, 2023, 17, 1239-1246.
41. N. Balke, S. M. Neumayer, J. A. Brehm, M. A. Susner, B. J. Rodriguez, S. Jesse, S. V. Kalinin, S. T. Pantelides, M. A. McGuire and P. Maksymovych, ACS Appl. Mater. Interfaces, 2018, 10, 27188-27194.
42. G. Kresse and J. Furthmüller, Comput. Mater. Sci, 1996, 6, 15-50.
43. V. Migliorati, A. Serva, F. M. Terenzio and P. D'Angelo, Inorg. Chem., 2017, 56, 6214-6224.

Materials Horizons Accepted Manuscript

View Article Online
DOI: 10.1039/D6MH00443A

44. R. A. Buckingham, Proc. R. Soc. Lond. A., 1938, 168, 264-283.
45. H. Yan, B. Wang, X. Yan, Q. Guan, H. Chen, Z. Shu, D. Wen and Y. Cai, Mater. Today Energy., 2022, 27, 101038.
46. Y. Cai, G. Zhang and Y.-W. Zhang, J. Phys. Chem. C., 2015, 119, 13929-13936.
47. J. Qi, H. Han, S. Yang, L. Kang, H. Yin and G. Zhao, Appl. Phys. Lett., 2024, 125.
48. R. He, H. Wang, F. Liu, S. Liu, H. Liu and Z. Zhong, Phys. Rev. B, 2023, 108, 024305.
49. Y. Liang, S. Shen, B. Huang, Y. Dai and Y. Ma, Mater. Horiz., 2021, 8, 1683-1689.
50. Y. Chen, X. Wang, L. Huang, X. Wang, W. Jiang, Z. Wang, P. Wang, B. Wu, T. Lin and H. Shen, Nat. Commun., 2021, 12, 4030.
51. C. Pan, A. Shi, X. Zhang, Y.-N. Wu, Y. Li and X. Niu, Phys. Rev. B, 2024, 110, 085406.
52. P. Singh, S. Baek, H. H. Yoo, J. Niu, J.-H. Park and S. Lee, ACS Nano, 2022, 16, 5418-5426.
53. Z. Zheng, Q. Ma, Z. Bi, S. de La Barrera, M.-H. Liu, N. Mao, Y. Zhang, N. Kiper, K. Watanabe and T. Taniguchi, Nature, 2020, 588, 71-76.
54. J. Huang, C. Ke, Z. Qian and S. Liu, Nano Lett., 2024, 24, 6683-6688.
55. Z. Zhang, P.-N. Roy, H. Li, M. Avdeev and L. F. Nazar, J. Am. Chem. Soc., 2019, 141, 19360-19372.
56. Y. Liu, A. N. Morozovska, A. Ghosh, K. P. Kelley, E. A. Eliseev, J. Yao, Y. Liu and S. Kalinin, ACS Nano, 2023, 17, 22004-22014.
57. C. Chen, H. Liu, Q. Lai, X. Mao, J. Fu, Z. Fu and H. Zeng, Nano Lett., 2022, 22, 3275-3282.
58. B. Wang, H. Yan, J. Huang, X. Yan, C. Huan, J. Lischner, Q. Ke and Y. Cai, Sci. Adv., 2026, 12, eaee1289.
59. T. Morawietz, O. Marsalek, S. R. Pattenaude, L. M. Streacker, D. Ben-Amotz and T. E. Markland, J. Phys. Chem. Lett., 2018, 9, 851-857.

Open Access Article. Published on 11 June 2026. Downloaded on 6/11/2026 11:35:10 PM.
This article is licensed under a Creative Commons Attribution-NonCommercial 3.0 Unported Licence.

Materials Horizons Accepted Manuscript

View Article Online
DOI: 10.1039/D6MH00443A

60. L. Pejov, P. Makreski and G. Jovanovski, Minerals, 2024, 14, 118.

Open Access Article. Published on 11 June 2026. Downloaded on 6/11/2026 11:35:10 PM.
This article is licensed under a Creative Commons Attribution-NonCommercial 3.0 Unported Licence.

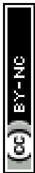

Materials Horizons Accepted Manuscript